Hantian Zheng, 23404940

Quantifying the Accumulation and Spatial Distribution of Molecular Hallmarks in the Subiculum of Alzheimer's Disease

By

Hantian Zheng

A THESIS SUBMITTED IN PARTIAL FULFILLMENT OF

THE REQUIREMENTS FOR THE DEGREE OF

BACHELOR OF SCIENCE

in

THE FACULTY OF SCIENCE

(Combined Honours, Biology and Computer Science)

THE UNIVERSITY OF BRITISH COLUMBIA

April 2025

We accept this thesis as conforming to the required standard

_____

_____

_____

_____

_____

Abstract

Alzheimer's disease (AD) is a progressive neurodegenerative disorder characterized by the accumulation of amyloid-beta (Aβ) plaques and neuronal loss. The subiculum, a key hippocampal output structure, is among the earliest affected regions in AD, yet its role in disease progression remains underexplored. This study investigates the spatial and temporal dynamics of extracellular Aβ42 accumulation and neuronal loss in the subiculum of 5xFAD transgenic mice, a well-established AD model. Using immunofluorescence imaging and machine learning-based segmentation, I quantified plaque burden and neuronal density across proximal and distal subicular subregions at three disease stages (6 weeks, 10 weeks, and 6 months). My results reveal a progressive increase in extracellular Aβ42 deposition, with plaques predominantly accumulating in the proximal subiculum. Concurrently, neuronal loss was most pronounced in the proximal subiculum, suggesting region-specific vulnerability. Regression analysis demonstrated a strong inverse correlation between Aβ42 plaque burden and neuronal density, reinforcing the link between Aβ pathology and neurodegeneration. These findings provide quantitative evidence of spatially distinct Aβ42 accumulation and neuronal loss in the subiculum, offering insights into AD progression and highlighting the need for region-specific therapeutic strategies.

Introduction

Alzheimer's disease (AD) is an irreversible, chronic, neurodegenerative disease that systematically destroys brain cells and remains the predominant cause of dementia. This devastating condition progressively impairs cognitive abilities and gradually erodes an individual's independence in daily functioning. By 2020, there were around 50 million AD patients worldwide, and this number is estimated to double every 5 years and reach 152 million by 2050 (Breijyeh & Karaman, 2020). Despite extensive research, contemporary medical interventions remain limited, providing only temporary symptomatic relief and cognitive stabilization without addressing the fundamental pathological mechanisms underlying the disease (Moreta et al., 2021).

AD is considered multifactorial, and one of the main hypotheses proposed to cause AD is the amyloid hypothesis (Breijyeh & Karaman, 2020). The amyloid hypothesis was originally proposed by George Glenner in 1984 and subsequently refined by neurogeneticist John Hardy

(Glenner & Wong, 1984; Hardy & Higgins, 1992; Selkoe & Hardy, 2016), and the hypothesis proposes an imbalance between the production and clearance of amyloid beta (Aβ) peptides is a very early, often initiating factor in AD. Since this discovery, the amyloid hypothesis has been the major target in the pharmaceutical industry, and this thesis is based on it.

While the amyloid hypothesis remains debated, Aβ dysregulation represents a critical upstream event in Alzheimer's pathogenesis. Even if Aβ accumulation is not the sole etiological factor, its early emergence (Selkoe & Hardy, 2016), strong correlation with cognitive decline (Chen et al., 2017), and mechanistic role in triggering downstream neurodegenerative cascades (Selkoe & Hardy, 2016) make it a pivotal therapeutic target.

5xFAD Mouse Model: Genetic Drivers of Aβ42 Overproduction

To study AD pathology in a controlled setting, various transgenic mouse models have been developed to recapitulate key aspects of the disease (Qian et al., 2024). The 5xFAD mouse model is a widely used and well-characterized model engineered to express five familial AD (FAD) mutations in amyloid precursor protein (APP) and presenilin 1 (PSEN1) genes (Oakley et al., 2006). This study selected this model primarily for two reasons. First, the 5xFAD model exhibits early and aggressive Aβ accumulation, with intracellular Aβ detected as early as 1.5 months, followed by the appearance of extracellular plaques in the subiculum by 2 months (Oakley et al., 2006). This is done via three amyloid precursor protein (APP) mutations (Swedish K670N/M671L, Florida I716V, and London V717I).

Aβ peptides are naturally occurring fragments produced through sequential proteolytic cleavage of amyloid precursor protein (APP) (Chen et al., 2017). APP is processed via two distinct pathways: the non-amyloidogenic pathway (dominant under physiological conditions) and the amyloidogenic pathway. In the latter, β-secretase first cleaves APP during its intracellular transport, followed by γ-secretase-mediated cleavage, generating Aβ peptides of varying lengths, predominantly Aβ40 and Aβ42 (Joshi & Wang, 2015). The three APP mutations in 5xFAD mice enhance the cleavage of APP by β-secretase (Swedish K670N/M671L) and γ-secretase (Florida I716V and London V717I). These peptides are either secreted into the extracellular space or retained at the plasma membrane, particularly within lipid rafts (Chen et al., 2017). Aβ monomers progressively aggregate into soluble oligomers, protofibrils, and ultimately insoluble fibrils that form amyloid plaques, a hallmark of AD. Aβ disrupts synaptic function through

multiple pathways. Soluble Aβ oligomers bind to membrane receptors (e.g., NMDA receptors), lipids, and metal ions, inducing mitochondrial dysfunction, oxidative stress, and calcium dyshomeostasis. Following receptor-mediated endocytosis, internalized Aβ accesses subcellular compartments via vesicular transport, where it interacts with organelles such as the endoplasmic reticulum (ER) and mitochondria, triggering ER stress and mitochondrial failure (Chen et al., 2017). Extracellularly, fibrillar Aβ deposits physically disrupt synapses and neurites, reducing synaptic density in affected brain regions. Given the accelerated pathology and Aβ accumulation, the 5xFAD model provides a valuable tool for investigating Aβ-related neurodegeneration in a limited time.

The second benefit of using the 5xFAD model is that it produces Aβ42 as the dominant form. Unlike other AD models, such as the APP/PS1 Model carrying only one PSEN1 mutation, producing mixed Aβ species (Qian et al., 2024), the 5xFAD model incorporates two PSEN1 mutations (M146L and L286V) that alter γ-secretase cleavage specificity, shifting APP processing toward Aβ42 to constitute >90% of total Aβ (Oakley et al., 2006), mirroring the Aβ42/Aβ40 ratio elevation observed in human AD brains. This is critical because Aβ42 is more neurotoxic and prone to plaque formation due to its extended hydrophobic C-terminal domain (Mawuenyeg et al., 2013).

The Subiculum as a Target Region

The subiculum, a pivotal output hub of the hippocampal formation, serves as a critical interface between the hippocampus and cortical/subcortical regions (Aggleton & Christiansen, 2015). Its bidirectional connectivity supports memory consolidation, spatial navigation, and contextual learning (Baset & Huang, 2024), functions that deteriorate early in AD (Ye et al., 2024). Notably, the subiculum comprises functionally distinct proximal and distal subdivisions (Fig. 1): Proximal pyramidal neurons (closer to CA1) encode local spatial cues through high-frequency bursting, while distal neurons (near the presubiculum) integrate global navigational signals via sustained firing (Cembrowski et al., 2018). This functional compartmentalization, characterized by differential gene expression, makes the subiculum an interesting target for studying its vulnerabilities to AD pathology.

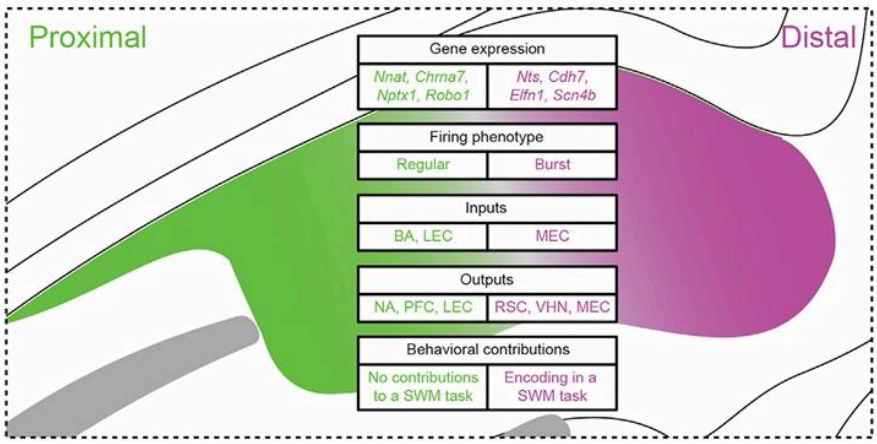

Figure 1. Differences between Proximal and Distal Subiculum Pyramidal Cells (Cembrowski et al., 2018).

Emerging evidence positions the subiculum as one of the earliest AD-affected regions, with atrophy detectable in presymptomatic stages (Carlesimo et al., 2015; Ye et al., 2024). Volumetric studies reveal progressive shrinkage in the presubiculum and subiculum that correlates with cognitive decline (Zhao et al., 2019), while tau pathology and neuronal loss in these regions precede hippocampal degeneration (La Joie et al., 2013). Despite this, most AD research focuses on the hippocampus, leaving unresolved whether Aβ42 accumulation respects the subiculum's functional subdivisions or diffusely targets the entire structure.

Given its early vulnerability, specific subdivisions, and role in cognitive functions, the subiculum provides an ideal model to investigate spatially patterned neurodegeneration in AD. This study uses the 5xFAD mouse model to map Aβ42 pathology onto the subiculum's proximal-distal axis.

Research Objectives

While prior studies established age- and sex-dependent amyloid deposition patterns in the subiculum of 5xFAD mice (Ye et al., 2024), critical gaps remain. Preliminary observations in 5xFAD mice (10 weeks and 6 months) from our lab revealed a qualitative association between extracellular Aβ42 accumulation and neuronal loss, but the quantitative spatial data on Aβ42 deposition was lacking. Furthermore, no studies systematically correlated extracellular Aβ42 burden with neuronal loss across AD progression stages or tested whether Aβ42 pathology preferentially targets the subiculum's functionally distinct proximal and distal subregions, which are domains critical for local vs. global cognitive processing (Cembrowski et al., 2018).

I hypothesized that extracellular Aβ42 accumulation increases with AD progression in 5xFAD mice, driving subregion-specific neuronal loss, particularly in the proximal subiculum, due to Aβ42's neurotoxicity (Mawuenyeg et al., 2013). To test this, I mapped and quantified extracellular Aβ42 plaque distribution across proximal vs. distal subiculum at three disease stages (6 weeks, 10 weeks, 6 months). In addition, I determined whether neuronal loss correlates temporally and spatially with Aβ42 burden in each subregion.

Results

Histological Progression of Aβ42 Pathology and Neuronal Loss

To find patterns of Aβ42 pathology, I analyzed 5xFAD mice at three disease stages (6 weeks, 10 weeks, and 6 months) using Aβ42 and NeuN immunofluorescence. Confocal imaging of 30 μm free-floating sections (63×, 0.5 μm z-steps) revealed observable age-dependent changes in plaque deposition and neuronal density (Fig. 2). At 6 weeks, Aβ42 immunoreactivity was predominantly intracellular, with staining overlapping NeuN+ neuronal somata (Fig. 2A), consistent with early intraneuronal Aβ42 accumulation (Oakley et al., 2006). No fibrillar plaques were observed, and neuronal density remained uniform across subicular subregions. By 10 weeks, small extracellular Aβ42 plaques emerged (Fig. 2B, middle), though neuronal loss in the subiculum pyramidal cell layer was minimal. At 6 months, dense Aβ42 plaques dominated the subiculum (Fig. 2C), with large aggregates (>50 μm diameter) displacing NeuN+ neurons. Autofluorescence from mature plaques obscured nearby NeuN signals (Fig. 2C, bottom), complicating neuronal quantification in plaque-dense areas. The proximal subiculum exhibited a

high plaque burden compared to distal subregions (Fig. 2C, middle, proximal-left vs. distal-right), mirroring patterns of neuronal loss.

These observations establish a qualitative spatiotemporal progression of Aβ42 pathology in the 5xFAD subiculum, with proximal subregions showing more severe plaque accumulation, which is a pattern that may reflect subregion-specific differences in Aβ clearance or neuronal vulnerability.

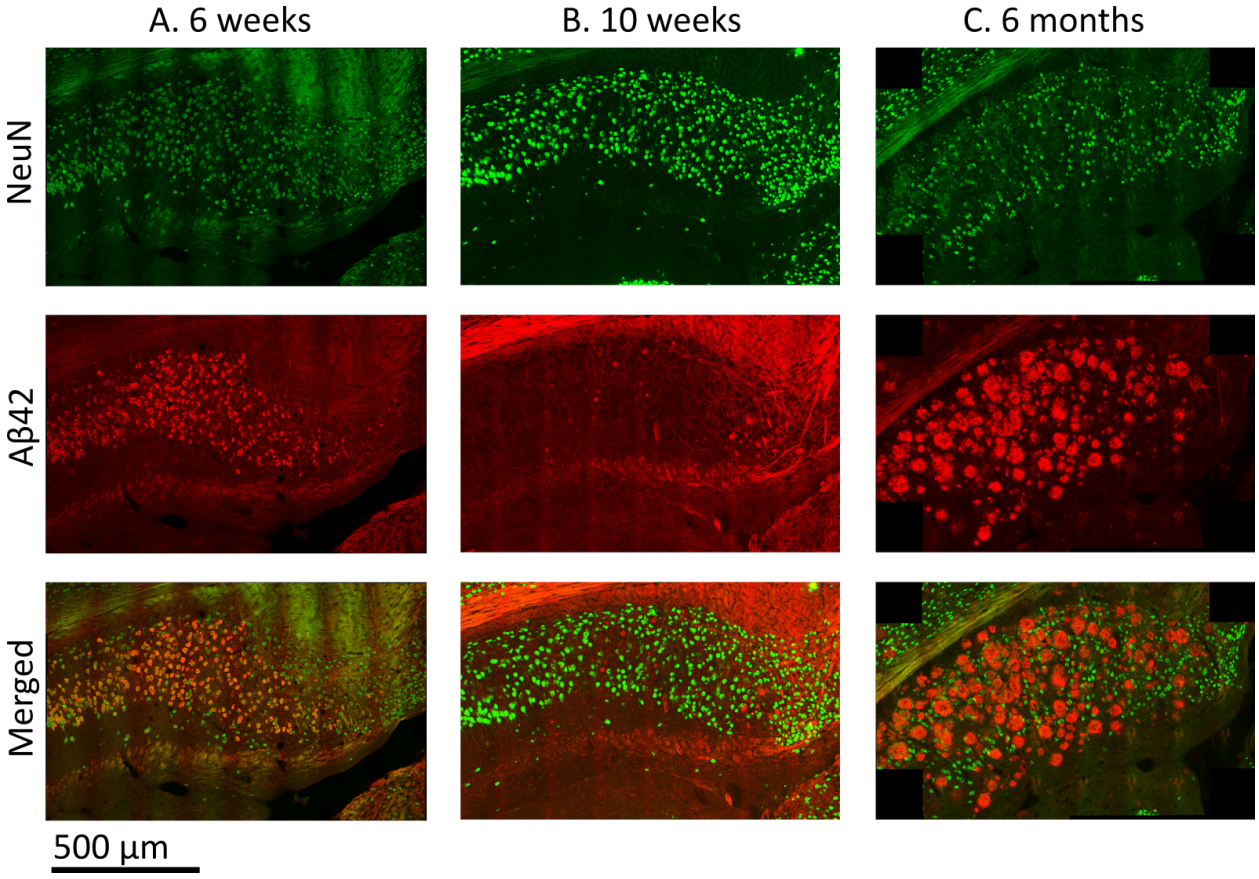

Figure 2. Age-dependent progression of Aβ42 plaques and neuronal loss in 5xFAD subiculum. (Top: NeuN; Middle: Aβ42; Bottom: Merge) (A) 6-week subiculum (ID: 01-6w-f): Intracellular Aβ42 (red) locates within neurons (green). (B) 10-week subiculum (ID: 04-10w-m): Small extracellular plaques with minimum neuronal loss. (C) 6-month subiculum (ID: 08-6m-m): Dense Aβ42 plaques with proximal predominance (left) and neuronal loss. Scale bar = 500 µm.

Spatial Mapping of Aβ42 and Neurons via Computational Segmentation

To quantify spatiotemporal relationships, I segmented Aβ42 plaques and neurons from confocal z-stacks using Cellpose v3 (Fig. 3). Raw immunofluorescence channels (NeuN: Fig. 3A1; Aβ42: Fig. 3B1) were processed into binary masks (Fig. 3A2, 3B2), where each colorful mask represent a neuron or plaque, each given a distinct ID. This binary segmentation allows more computations on individual plaques and neurons across all ages, including mask counts, centroid locations, and the area of each mask in the figures. Segmentation accuracy was validated against manual counts.

Morphometric data (plaques: area/μm^2; neurons: count/μm^2) were mapped to proximal-distal subregions using a Cartesian coordinate system normalized to individual subiculum anatomy (Fig. 3A3–A4, 3B3–B4). A midline division (red) separated subregions, consistent with anatomical definitions (Cembrowski et al., 2018), and the masks in the proximal/distal subiculum were plotted as distinctively colored dots for visualization. Both Aβ42 plaques and NeuN+ neurons localized predominantly to deeper subicular layers (above the black boundary line marking subiculum borders). Notably, proximal subiculum exhibited greater Aβ42 deposition compared to distal regions (Fig. 3B3–B4).

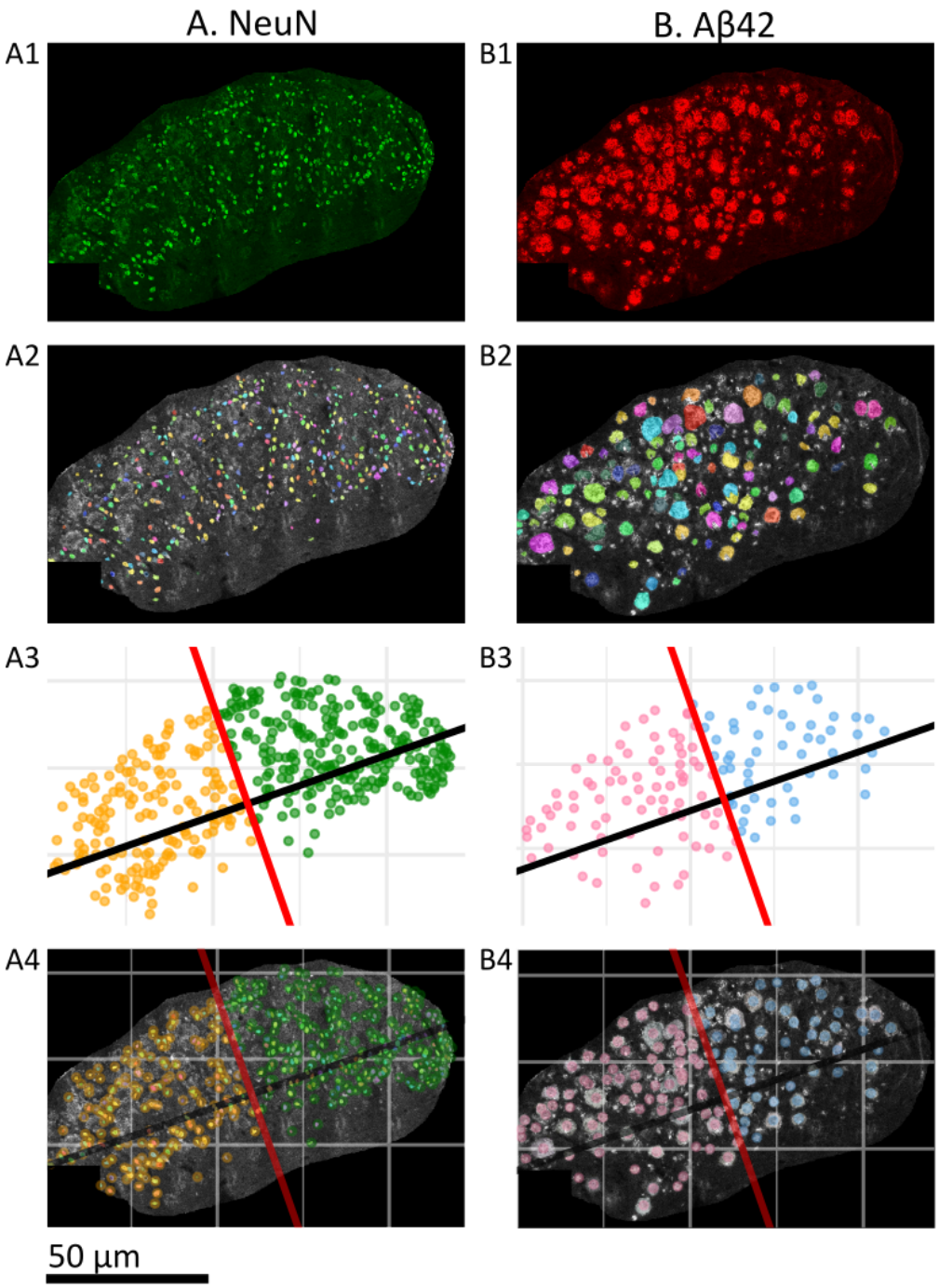

Figure 3. Segmentation workflow for spatial analysis (ID: 08-6m-m). (A) Neurons (NeuN channel). A1: Raw confocal image with manually selected subiculum. **A2**: Cellpose-derived NeuN+ nuclei segmentation. **A3–A4**: Proximal (left of midline) and distal subregions mapped via spatial coordinates. **(B) Plaques (Aβ42 channel). B1**: Raw confocal image of Aβ42 with subiculum selection. **B2**: Cellpose-derived Aβ42+ plaque segmentation. **B3–B4**: Proximal/distal subregions mapped as in A3–A4. Scale bar = 50 µm.

Age-Dependent Extracellular Plaque Accumulation

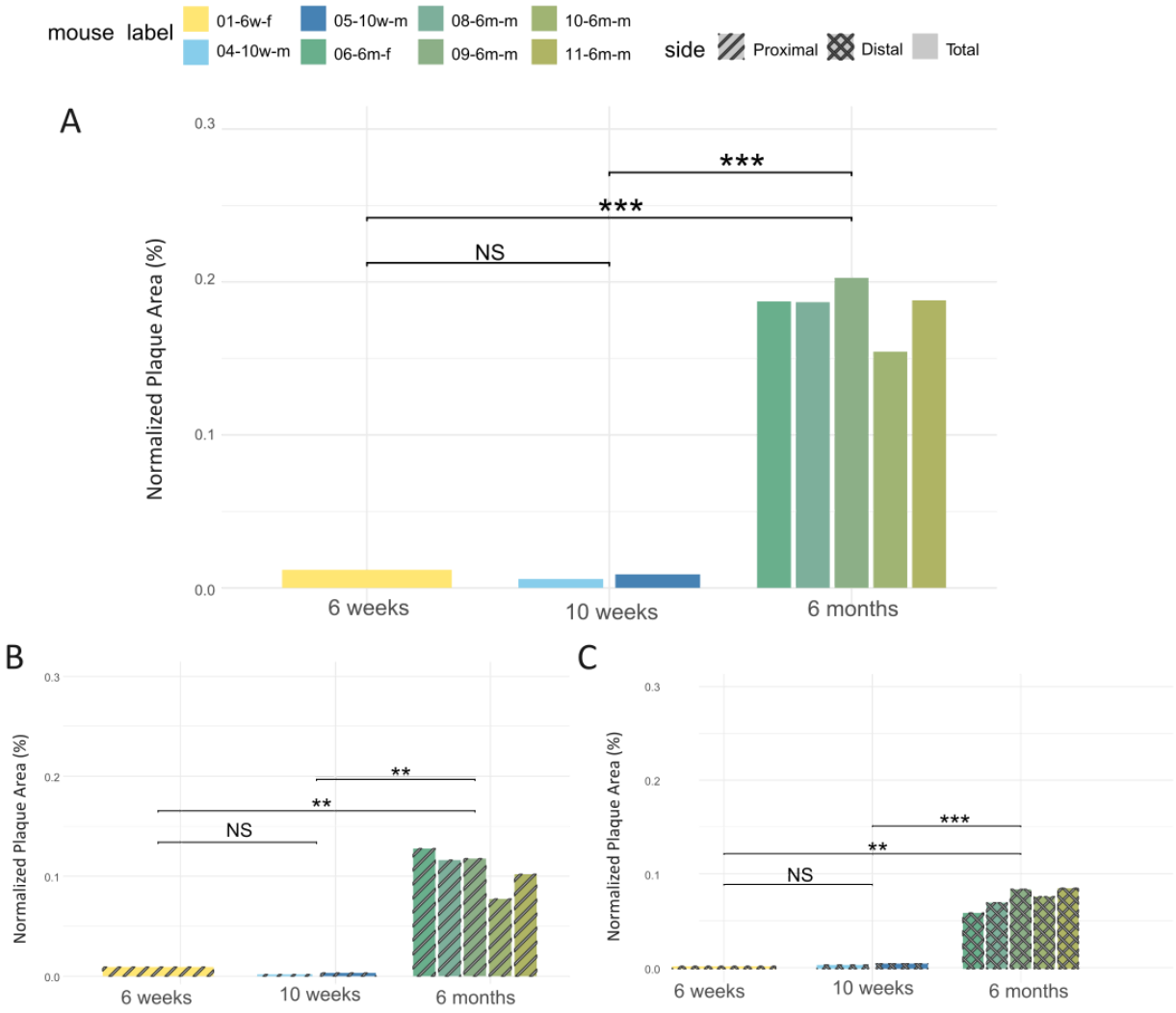

Figure 4. Normalized plaque accumulation across age groups. (A) Global subiculum **(B)** Proximal subiculum **(C)** Distal subiculum. Significance levels: $p < 0.001$, $p < 0.01$, $p < 0.05$; NS = not significant ($p \geq 0.05$).

Global analysis revealed a system-wide surge in plaque burden by 6 months (ANOVA: $F(2,5) = 113.86$, $p < 0.0001$), exceeding younger groups by 17% ($p < 0.001$) (Fig. 4A, Table 1). The proximal subiculum exhibited dramatic age-dependent plaque expansion (ANOVA: $F(2,5) = 32.89$, $p = 0.0013$), with 6-month-old mice showing 9.9% greater normalized plaque area compared to 6-week controls ($p = 0.008$) and 10.6% more than 10-week-old mice ($p = 0.002$) (Fig. 4B). While the distal subiculum followed a similar temporal progression, its plaque

accumulation was less pronounced (ANOVA: $F(2,5) = 50.24$, $p < 0.001$), with significant increases only at 6 months (+7.3% vs. 6-week, $p = 0.002$; +7.1% vs. 10-week, $p = 0.0008$) (Fig. 4C). Age accounted for >90% of variance in plaque accumulation across all subregions ($\eta^2 > 0.90$, Table 1), revealing its dominant role in amyloid pathology.

Table 1. Age-related differences in normalized plaque area

Subregion	*F*(df)	*p-value*	η^2	Key Comparisons (Tukey HSD)
Total	*F*(2,5)=113.9	<0.001	0.98	6m < 6w (p<0.001), 6m < 10w (p<0.001)
Proximal	*F*(2,5)=32.9	0.001	0.93	6m < 6w (p=0.008), 6m < 10w (p=0.002)
Distal	*F*(2,5)=50.2	<0.001	0.95	6m < 6w (p=0.002), 6m < 10w (p=0.001)

Age-Dependent Neuronal Loss

Global neuron density declined significantly with age (ANOVA: $F(2,5) = 25.4$, $p = 0.002$, Fig. 5A), decreasing by 28.1% at 6 months compared to 10-week-old mice ($p = 0.004$; Table 2). This system-wide neurodegeneration was driven predominantly by severe neuronal loss in the proximal subiculum pyramidal cell layer ($F(2,5) = 37.3$, $p = 0.001$), where 6-month density plummeted by 31.5% vs. 6-week controls ($p < 0.001$; Fig. 5B). In contrast, the distal subiculum showed milder reductions, which is 16.4% lower than 6-week controls ($p = 0.115$) but 26.7% lower than 10-week-old mice ($p = 0.007$; Fig. 5C). Age accounted for >85% of variance across all subregions ($\eta^2 > 0.86$), with proximal areas exhibiting the most pronounced decline (Table 2). Global neuronal counts in the subiculum decrease with age, and proximal subregions exhibit a greater neuron loss, showing a pattern mirroring Aβ42 plaque accumulation and underscoring regional vulnerability in AD.

Table 2. Age-related differences in normalized neuron density

Subregion	*F*(df)	*p-value*	η^2	Key Comparisons (Tukey HSD)
Total	*F*(2,5)=25.4	0.002**	0.91	6m < 6w (*p*=0.009), 6m < 10w (*p*=0.004)
Proximal	*F*(2,5)=37.3	0.001**	0.94	6m < 6w (*p*=0.001), 6m < 10w (*p*=0.006)
Distal	*F*(2,5)=15.1	0.008*	0.86	6m < 10w (*p*=0.007)

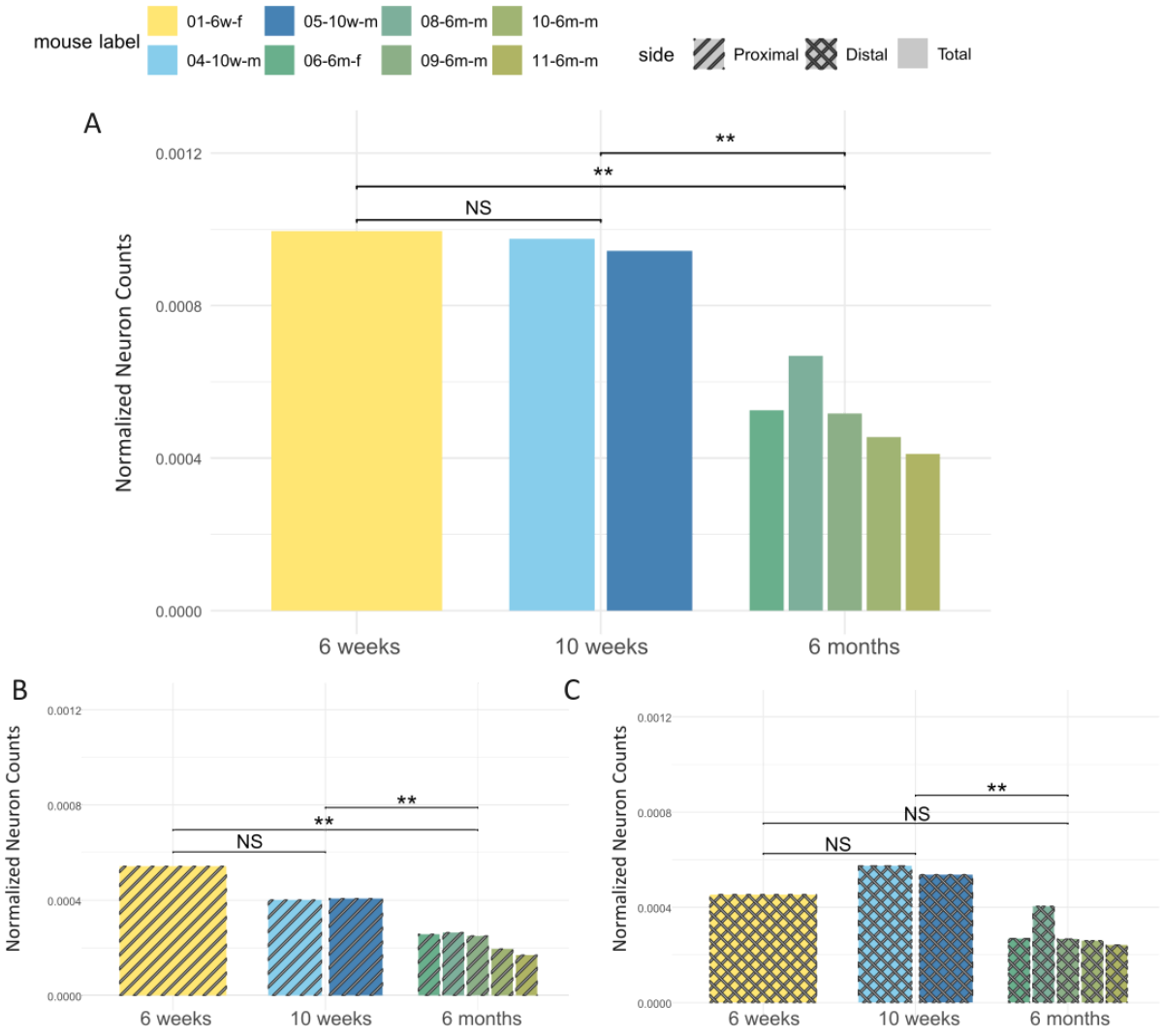

Figure 5. Normalized neuron density across age groups. (A) Global subiculum **(B)** Proximal subiculum **(C)** Distal subiculum Significance levels: *p < 0.001, p < 0.01, *p < 0.05; NS = not significant (p ≥ 0.05).

Proximal-Distal Plaque and Neuron Distribution

To isolate spatial differences in Aβ42 and neuronal distribution from age-related effects, I performed paired analyses on 6-month-old mice (Fig. 6). For the plaque distribution, Shapiro-Wilk tests confirmed normality, allowing paired t-tests. Proximal subiculum showed higher plaque burden compared to distal regions ($p = 0.0503$; Fig. 6A). While marginally significant, all mice exhibited proximal dominance (individual trajectories, Fig. 6A), suggesting biological relevance requiring validation in larger size of samples. Similarly, paired t-tests were performed on NeuN+ counts. The distal subiculum showed near-significant neuronal sparing ($p = 0.0580$; Fig. 6B), with all pairs favoring distal regions. The exact p-values consistency imply potential subregion-specific resilience masked by limited sample size.

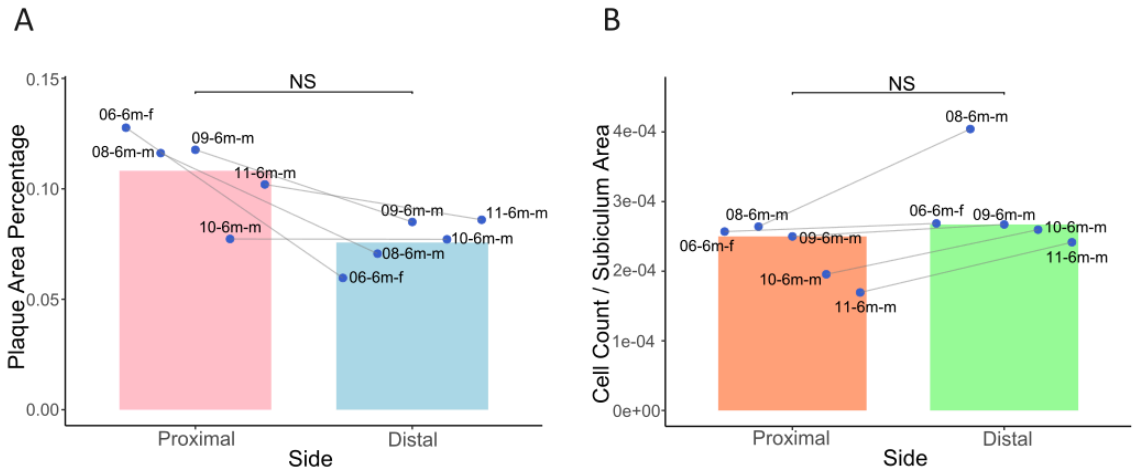

Figure 6. Spatial distribution of Aβ42 plaques and neurons in 6-month subiculum. (A) Plaque area: Proximal vs. distal ($p = 0.0503$, paired t-test). **(B)** Neuron density: Proximal vs. distal ($p = 0.0580$, paired t-test). Gray lines: Individual paired trajectories. Significance thresholds: $p < 0.05$ (*), NS = not significant ($p \geq 0.05$).

Neuron-Plaque Spatial Anticorrelation

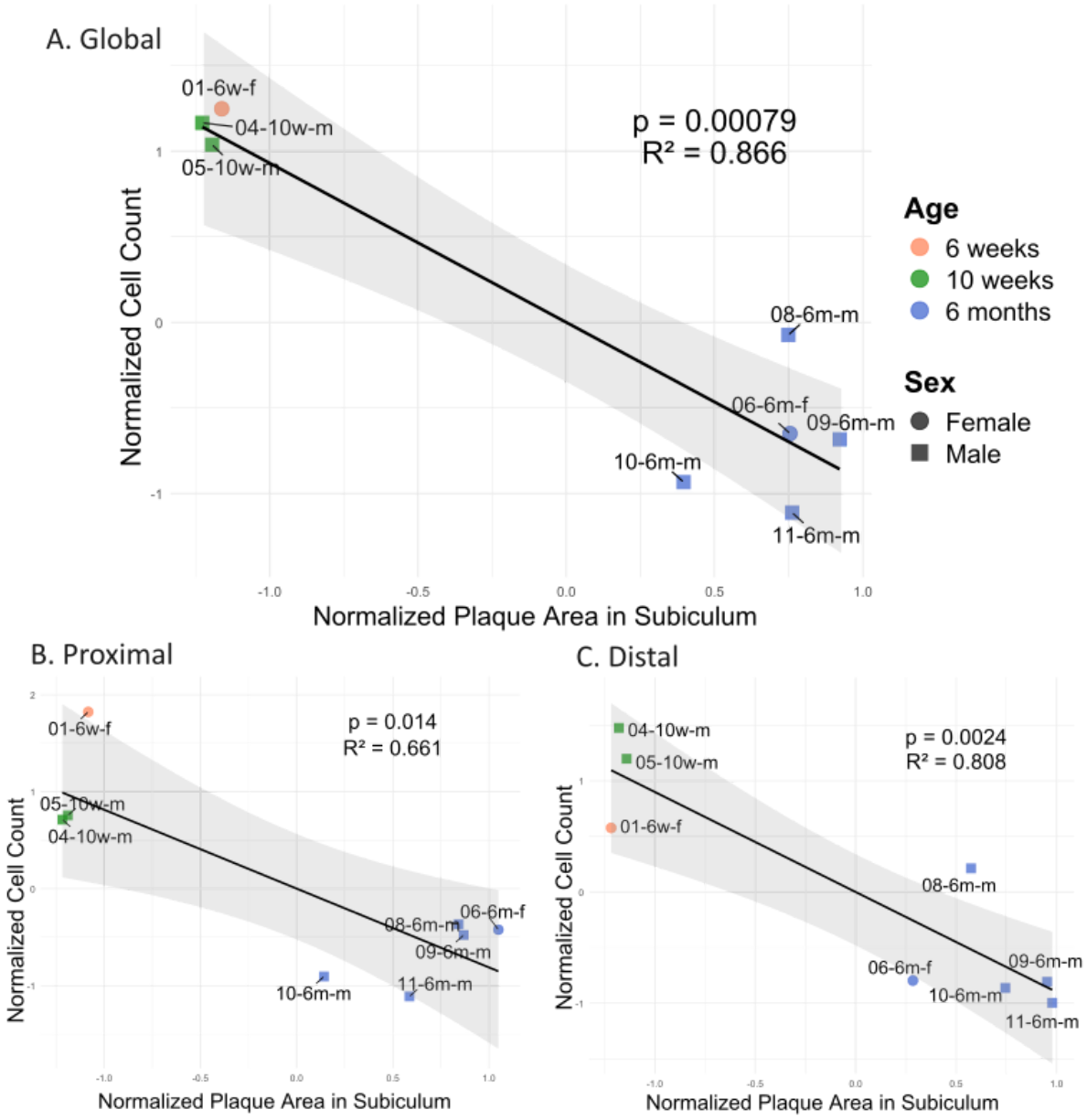

Figure 7. Inverse relationship between neuronal density and plaque accumulation. (A) Global subiculum ($p = 0.00079$, $R^2 = 0.866$, $\beta = -0.931$). (B) Proximal subiculum ($p = 0.0142$, $R^2 = 0.661$, $\beta = -0.813$). (C) Distal subiculum ($p = 0.0024$, $R^2 = 0.808$, $\beta = -0.899$). Scatterplots show normalized values (Z-scores) across ages (6 weeks = orange, 10 weeks = green, 6 months = blue) and sex (female = circles, male = squares). Solid line: linear fit; shaded band: 95% CI. Individual IDs annotated.

Whole-subiculum linear regression revealed a strong inverse relationship between plaque burden and neuron density ($p=0.0008$; Fig. 7A). The model exhibited high explanatory power ($R^2 = 0.866$), indicating that plaque burden accounts for 86.6% of neuronal density variance. A one standard deviation (SD) increase in AB plaque area (9.16 percentage points) was associated with a 0.93 SD decrease in neuronal density. In absolute terms, this corresponds to a reduction of 0.00023 neurons/μm² (0.93 × 0.000248 neurons/μm²). For a 6-month-old mouse subiculum area of 0.5 mm² (500,000 μm²), this equates to a loss of approximately 115 neurons (0.00023 neurons/μm² × 500,000 μm²). Age-based clustering was evident: 6-week (orange) and 10-week (green) mice occupied the high-neuron/low-plaque quadrant, while 6-month mice (blue) clustered in the low-neuron/high-plaque quadrant (Fig. 7A). The subdivision analysis (proximal: $R^2 = 0.661$, $\beta = -0.813$; distal: $R^2 = 0.808$, $\beta = -0.899$) demonstrated a weaker but still strong inverse plaque-neuron relationship compared to global subiculum. The robust inverse correlation between Aβ42 plaques and neuronal density, particularly in the proximal subiculum, supports an important role for amyloid pathology in driving neurodegeneration, offering a quantitative framework to evaluate future therapeutic strategies.

Discussion

This study systematically demonstrates a spatiotemporal progression of Aβ42 pathology and neuronal loss in the 5xFAD subiculum, revealing three critical insights: (1) from 6 weeks to 6 months, Aβ42 transits from intracellular space to extracellular space and accumulates over time, while neuron counts decrease significantly at 6 months (Figs. 2-5); (2) proximal subiculum exhibits more severe Aβ42 accumulation and neurodegeneration (Fig. 6); (3) plaque burden inversely correlates with neuronal density, with proximal regions showing the strongest anticorrelation (Fig. 7). Below, I interpret these findings in the context of AD mechanisms.

The histological progression in 5xFAD mouse subiculum (Fig. 2) aligns with studies showing early intraneuronal Aβ42 accumulation preceding extracellular plaques. At 6 weeks, intracellular Aβ42 locates within NeuN+ neurons (Fig. 2A), consistent with Oakley et al. (2006). At 10 weeks, there are very few extracellular Aβ42 deposition (Fig. 2B). By 6 months, dense extracellular Aβ42 plaques accumulate in the subiculum (Figs. 2C, 3), exhibiting significantly larger areas compared to younger mice globally and across all subregions (Fig. 4), and neuronal density has declined markedly at 6 months (Fig. 5). These findings are consistent with the

amyloid cascade hypothesis (Selkoe & Hardy, 2016), and the plaques displace neurons which is consistent with the finding that extracellular Aβ42 disrupts synaptic plasticity as fibrillar aggregates (Chen et al., 2017).

The spatial pattern of plaque accumulation and neuronal loss across the subiculum is striking. Interestingly, the proximal subiculum showed greater vulnerability to amyloid pathology than the distal region, with neuronal loss being nearly twice as pronounced in the proximal area (31.5% vs. 16.4% loss; Fig. 5B-C). At 6 months of age, direct comparisons between subregions revealed trends toward higher plaque burden (proximal: $p = 0.0503$, paired t-test; Fig. 6A) and greater neuronal loss ($p = 0.0580$, paired t-test; Fig. 6B), which approached but did not reach conventional statistical significance. These borderline findings call for cautious interpretation, as the small sample size ($n = 5$ mice) increases the risk of overinterpreting preliminary trends. However, the consistent directional patterns of higher plaques and lower neurons in the proximal subiculum imply biologically meaningful regional vulnerability. Follow-up studies in larger cohorts will help clarify whether these subtle differences reflect true pathological specificity.

The observed proximal-distal vulnerability differences may arise through multiple mechanisms. First, the proximal subiculum demonstrates a closer connectivity with AD-vulnerable regions like the entorhinal cortex (Aggleton & Christiansen, 2015; Ye et al., 2024), potentially creating a feedforward loop where early entorhinal pathology propagates Aβ42 toxicity via hyperactive neural circuits. This network architecture could expose proximal neurons to heightened Aβ42 exposure through both local production and anterograde transmission from connected regions. Second, pyramidal cells in proximal subregions exhibit distinct molecular profiles, including elevated expression of synaptic plasticity regulators like Nptx1 (Cembrowski et al., 2018). These intrinsic differences may render proximal neurons more susceptible to Aβ oligomer-induced excitotoxicity through mechanisms involving AMPA receptor clustering and calcium dysregulation (Chen et al., 2017).

However, the cross-sectional data from 6-month-old mice cannot conclusively distinguish whether proximal subregions possess inherent biological vulnerability to Aβ42 toxicity or simply reach pathological thresholds earlier in the disease cascade due to temporal progression gradients. The current findings reflect end-stage pathology in this accelerated 5xFAD model.

Longitudinal tracking of Aβ42 deposition kinetics and neuronal survival across subregions will be required to resolve this temporal vs. spatial vulnerability distinction.

The near 1:1 inverse relationship between plaque burden and neuronal density (R^2=0.866 globally; R^2=0.661 proximally; R^2=0.808 distally; Fig. 7) quantitatively supports Aβ42's neurotoxic role (Mawuenyeg et al., 2013). While the standardized coefficient ($\beta = -0.93$ globally; Fig. 7A) indicates a robust statistical relationship, the small absolute decrease in neuronal density (0.00023 neurons/μm^2) warrants careful interpretation. This apparent subtlety arises from the scale of measurement since neuronal density was measured as neurons per micrometer squared, a unit inherently small due to the subiculum's microscopic scale. When scaled to biologically meaningful areas (e.g., a subiculum size, 0.5 mm^2), the effect translates to a loss of ~115 neurons per SD increase in plaque burden, which may represent substantial regional neurodegeneration. Such a strong correlation is also observed in both subregions (Fig. 7B-C), though the global subiculum analysis demonstrated a stronger inverse plaque-neuron relationship compared to subdivisions. This discrepancy highlights the methodological impact of spatial resolution on neurodegenerative analyses. Global measurements integrate signals across larger areas, diluting noise and amplifying effect detectability. Conversely, subdivisions, while biologically meaningful, introduce granular variability (e.g., cell density fluctuations, focal Aβ deposition patterns) that reduce model performance. This aligns with neuroimaging studies, where regional atrophy measures often show weaker effect sizes than whole-brain metrics due to increased spatial specificity.

This anticorrelation reinforces previous studies that have linked Aβ dyshomeostasis to synaptic dysfunction, mitochondrial impairment, and ultimately, cell death (Mawuenyega et al., 2013; Chen et al., 2017). One possible mechanism to explain the relation between higher Aβ deposition and reduced neuron density can involve Nptx1. As Aβ plaques preferentially deposit in the proximal subiculum, these Aβ oligomers transcriptionally upregulate NPTX1 (Abad et al., 2006), and an enhanced transcription of Nptx1 in the proximal subiculum was also evidenced by popRNA-seq experiments in WT mice (Cembrowski et al., 2018). The NPTX1 overexpression significantly increased AMPA receptor clustering, resulting in excitatory synapses (Xu et al., 2003). Since AMPA receptors allow Ca2+ influx, followed by mitochondrial calcium overload, and this can lead to oxidative stress-induced neuronal cell damage and death (Beattie et al., 2010; Calvo-Rodriguez et al., 2024).

While my findings are robust, several limitations warrant consideration. The cross-sectional design captures static snapshots rather than longitudinal progression, potentially missing individual trajectories of plaque accumulation and neuronal loss. Small sample sizes and sex imbalance limit generalizability. Female 5xFAD mice often exhibit accelerated Aβ pathology (Ye et al., 2024), yet my samples lacked sufficient females for sex-specific analysis. Additionally, the 5xFAD model's aggressive pathology (6 months vs. human decades) may overemphasize Aβ42's role while compressing neurodegeneration timelines that normally unfold over years in humans. This temporal compression limits our ability to study dynamic interactions between early intracellular Aβ accumulation and later extracellular plaque formation. In contrast, APP Knock-in Models (e.g., APPNL-G-F), which exhibit slower Aβ accumulation and age-dependent pathology without the artificial γ-secretase bias toward Aβ42 seen in 5xFAD, may better reflect human AD progression (Qian et al., 2024). Besides, the potential variability in the expression of the five AD-related mutations within the 5xFAD model may have contributed to the observed heterogeneity in plaque and neuronal measures.

Future studies should address these limitations through longitudinal tracking of Aβ42 deposition and neuronal populations in vivo using multiphoton imaging or PET-MRI, enabling observation of spatiotemporal progression patterns in individual animals. To test the proposed mechanism of Aβ42/neuron anticorrelation mentioned above, time-resolved spatial transcriptomics could map NPTX1 expression dynamics relative to plaque development in proximal vs. distal subiculum. Combination therapies might integrate Aβ clearance strategies (e.g., anti-Aβ antibodies) with neuroprotective agents targeting Ca^{2+} dysregulation, with treatment timing guided by longitudinal biomarker monitoring.

In summary, the study provides compelling evidence that progressive Aβ42 accumulation in the subiculum is closely associated with neuronal loss in the 5xFAD mouse model of AD. The spatially distinct patterns of pathology observed between proximal and distal subregions revealed the complexity of AD pathogenesis and suggest that targeted therapeutic interventions may need to account for regional differences in vulnerability. Continued research into the molecular drivers of this differential susceptibility is essential for the development of effective disease-modifying strategies.

Methods

Methods Table

REAGENT or RESOURCE	SOURCE	IDENTIFIER
Antibodies		
Beta-Amyloid (1-42) Monoclonal Antibody (GT622)	Thermo Scientific	MA5-36246
Vectashield Mounting Medium with DAPI	BioLynx	VECTH1500
NeuN (D4G4O) XP® Rabbit mAb	Cell Signaling Technology	#24307
Goat anti-Mouse IgG2b Cross-Adsorbed Secondary Antibody, Alexa Fluor™ 647	Thermo Scientific	A-21242
Goat anti-Rabbit IgG (H+L) Highly Cross-Adsorbed Secondary Antibody, Alexa Fluor™ 568	Thermo Scientific	A-11036
Chemicals, Peptides, and Recombinant Proteins		
Phosphate Buffered Saline (PBS)	Fisher BioReagents	BP665-1
paraformaldehyde (PFA)	Electron Microscopy Sciences	15710
Sucrose	Sigma-Aldrich	S7903-1KG
Triton X-100	Sigma	T8787-50mL
Normal Goat Serum (NGS)	Abcam	ab7481
Deposited Data		
Raw and analyzed data	this thesis	https://github.com/zhengmiaa/BIOL_449
Experimental Models: Organisms/Strains		
Mouse: B6.Cg-Tg (APPSwFlLon, PSEN1*M146L*L286V) 6799Vas/Mmjax	The Jackson Laboratory	MMRRC_034848-JAX
Software and Algorithms		
ImageJ2	Rueden et al.	https://github.com/imagej/imagej2
Cellpose v3	Stringer et al.	https://github.com/MouseLand/cellpose
R version 4.1.1	R Core Team	https://cran.r-project.org/bin/windows/base/
Python	Python Software Foundation	https://www.python.org/
Other		
SP8 Leica white light laser confocal microscope	Leica Microsystems	N/A

Resource Availability

Lead Contact

Further information and requests should be directed to and will be fulfilled by the lead contact, Dr Mark S. Cembrowski (mark.cembrowski@ubc.ca).

Materials availability

This study did not generate unique reagents.

Data and code availability

The original code and any additional information required to reanalyze the data reported in this paper are available from the lead contact upon request.

Experimental Model and Subject Details

The study utilized 5xFAD transgenic mice, a widely used model for AD. Mice were aged 6 weeks, 10 weeks, or 6 months at the time of tissue collection, with both male and female animals included. Mice were housed in standard laboratory conditions with a 12-hour light/dark cycle, with food and water available ad libitum. All animal procedures were approved by the UBC Animal Care Committee and conducted in compliance with institutional and governmental regulations for the care and use of laboratory animals.

The 5xFAD model was selected due to its accelerated development of amyloid pathology, making it suitable for investigating the progression of AD and related changes in neuronal and plaque distributions.

Methods Details

Immunohistochemistry

5xFAD mice (B6.Cg-Tg(APPSwFlLon, PSEN1*M146L*L286V) 6799Vas/Mmjax), aged 6 weeks (1 female, 1 male), 10 weeks (2 males, 1 female), and 6 months (1 female, 5 males), were deeply anesthetized with isoflurane and perfused with 1 x phosphate-buffered saline (PBS), followed by 4% paraformaldehyde (PFA) in 1 x PBS. The brains were dissected, post-fixed in

4% PFA for 24 hours, and cryoprotected in 30% sucrose in 1 x PBS for approximately 48 hours. Subsequently, the brains were sectioned into 30 μm slices using a cryostat, stored as free-floating sections in 1× PBS, and kept at 4°C until further processing.

Immunohistochemical staining was performed on free-floating 30 μm fixed tissue sections. The sections were washed twice with 1× PBS for 15 minutes each and permeabilized with 0.3% Triton-X-100 in PBS (Triton-PBS) for two 15-minute washes. Sections were then incubated for 1 hour at room temperature in a blocking buffer consisting of 5% normal goat serum (NGS) in 0.3% Triton-PBS.

The tissue sections were incubated overnight at 4°C with the following primary antibody solution: Beta-Amyloid (1-42) Monoclonal Antibody (GT622) and NeuN (D4G4O) XP® Rabbit mAb, diluted in 0.3% Triton-PBS. After incubation, sections were washed three times for 10 minutes each in 0.3% Triton-PBS, followed by a 3–6 hour incubation at room temperature with Alexa Fluor secondary antibodies (Alexa Fluor™ 568 for NeuN and Alexa Fluor™ 647 for Beta-Amyloid (1-42)) diluted 1:500 in 0.3% Triton-PBS. Finally, the sections were washed three times in 1× PBS for 10 minutes each, mounted onto slides, and coverslipped with a mounting medium containing DAPI for nuclear staining.

Due to significantly lower image quality in comparison with others, a 6-week male (ID: 02-6w-m) and a 10-week female (ID: 03-10w-f) were excluded. A 6-month mouse (ID: 07-6m-m) was also excluded, being an outlier relative to other 6-month mice. It has double the number of neurons and fewer plaques, potentially due to incomplete genetic mutation, such as not carrying all of the five AD mutations.

Imaging

Images were captured using a 63× objective on an SP8 Leica white light laser confocal microscope. Z-stacks were acquired with a step size of 0.50 μm for each imaging session. Final composite images were generated as pseudo-colored maximum-intensity projections, with channels opaquely overlaid in order of highest to lowest expression. The presented images underwent uniform brightness adjustments applied consistently across individual channels. Image qualities were improved using ImageJ2, including brightness adjustments and pseudocoloring to facilitate cross-channel visual comparisons.

Image Segmentation

The multi-channel images were split into single channels, and the subiculum region was manually selected using ImageJ2 (Rueden et al., 2017). Immunofluorescence images of subiculum were processed using Cellpose v3 (Stringer et al., 2021), a deep learning-based segmentation framework. For neuronal nuclei segmentation, NeuN channel images were analyzed with the pretrained Cyto3 model using iterative refinement. Model training incorporated a learning rate of 0.1 with exponential decay, L2 regularization (weight decay=0.0001), and 100 training epochs. Aβ plaque segmentation employed the same Cyto3 architecture but required additional manual curation for younger cohorts (6- and 10-week-old mice) due to minimal extracellular deposits. Segmentation outputs generated 2D pixel matrices where background pixels were assigned 0, while unique integer IDs identified individual cellular structures.

Morphometric Quantification

Custom Python scripts (v3.9) converted pixel coordinates to micrometer-scale measurements using calibration data from Leica confocal microscope settings. Neuronal density was calculated as NeuN+ nuclei count per μm^2 subicular area, and Aβ deposition was calculated as the sum of Aβ staining areas per μm^2 subicular area. Particularly, since the 6-week-old mice have primarily intracellular Aβ staining, their extracellular Aβ deposition was measured by removing the overlapping region between Aβ and NeuN+ staining from Aβ stainings. Spatial distribution analyses utilized a Cartesian coordinate system normalized to individual subiculum morphology, with proximal/distal subdivisions defined relative to the midpoint between presubiculum and CA1 boundaries.

Statistical Analysis

All analyses were conducted in R v4.1.1. ANOVA with Tukey HSD posthoc testing compared age groups, while paired t-tests assessed proximal-distal differences. Linear regression models incorporated normalized plaque area as the predictor and neuronal density as the response variable. Effect sizes were reported using η^2 for ANOVA and standardized β coefficients for regression.

References

Abad, M. A., Enguita, M., DeGregorio-Rocasolano, N., Ferrer, I., & Trullas, R. (2006). Neuronal pentraxin 1 contributes to the neuronal damage evoked by amyloid-beta and is overexpressed in dystrophic neurites in Alzheimer's brain. *The Journal of neuroscience : the official journal of the Society for Neuroscience, 26*(49), 12735–12747. https://doi.org/10.1523/JNEUROSCI.0575-06.2006

Aggleton, J. P., & Christiansen, K. (2015). The subiculum: The heart of the extended hippocampal system. *Progress in Brain Research, 219*, 65-82. https://doi.org/10.1016/bs.pbr.2015.03.003

Baset, A., & Huang, F. (2024). Shedding light on subiculum's role in human brain disorders. *Brain Research Bulletin, 214*, 110993. https://doi.org/10.1016/j.brainresbull.2024.110993

Beattie, M. S., Ferguson, A. R., & Bresnahan, J. C. (2010). AMPA-receptor trafficking and injury-induced cell death. *The European Journal of Neuroscience, 32*(2), 290. https://doi.org/10.1111/j.1460-9568.2010.07343.x

Behl, C. (2024). In 2024, the amyloid-cascade-hypothesis still remains a working hypothesis, no less but certainly no more. *Frontiers in Aging Neuroscience, 16*, Article 1459224. https://doi.org/10.3389/fnagi.2024.1459224

Breijyeh, Z., & Karaman, R. (2020). Comprehensive review on Alzheimer's disease: Causes and treatment. *Molecules, 25*(24), Article 5789. https://doi.org/10.3390/molecules25245789

Carlesimo, G. A., Piras, F., Orfei, M. D., Iorio, M., Caltagirone, C., & Spalletta, G. (2015). Atrophy of presubiculum and subiculum is the earliest hippocampal anatomical marker of Alzheimer's disease. *Alzheimer's & Dementia: Diagnosis, Assessment & Disease Monitoring, 1*(1), 24-32. https://doi.org/10.1016/j.dadm.2014.12.001

Calvo-Rodriguez, M., Kharitonova, E. K., Snyder, A. C., Hou, S. S., Sanchez-Mico, M. V., Das, S., Fan, Z., Shirani, H., Nilsson, K. P. R., Serrano-Pozo, A., & Bacskai, B. J. (2024). Real-time imaging of mitochondrial redox reveals increased mitochondrial oxidative stress associated with amyloid β aggregates in vivo in a mouse model of Alzheimer's disease. *Molecular neurodegeneration, 19*(1), 6. https://doi.org/10.1186/s13024-024-00702-2

Cembrowski, M. S., Phillips, M. G., DiLisio, S. F., Shields, B. C., Winnubst, J., Chandrashekar, J., Bas, E., & Spruston, N. (2018). Dissociable Structural and Functional Hippocampal Outputs via Distinct Subiculum Cell Classes. *Cell*, *173*(5), 1280–1292.e18. https://doi.org/10.1016/j.cell.2018.03.031

Chen, G., Xu, T., Yan, Y., Zhou, Y., Jiang, Y., Melcher, K., & Xu, H. E. (2017). Amyloid beta: Structure, biology and structure-based therapeutic development. *Acta Pharmacologica Sinica, 38*(9), 1205–1235. https://doi.org/10.1038/aps.2017.28

Glenner, G. G., & Wong, C. W. (1984). Alzheimer's disease and Down's syndrome: Sharing of a unique cerebrovascular amyloid fibril protein. *Biochemical and Biophysical Research Communications, 122*(3), 1131–1135. https://doi.org/10.1016/0006-291X(84)91209-9

Hardy, J. A., & Higgins, G. A. (1992). Alzheimer's disease: The amyloid cascade hypothesis. *Science, 256*(5054), 184–185. https://doi.org/10.1126/science.1566067

Joshi, G., & Wang, Y. (2015). Golgi defects enhance APP amyloidogenic processing in Alzheimer's disease. *BioEssays : news and reviews in molecular, cellular and developmental biology*, *37*(3), 240–247. https://doi.org/10.1002/bies.201400116

La Joie, R., Perrotin, A., De La Sayette, V., Egret, S., Doeuvre, L., Belliard, S., Eustache, F., Desgranges, B., & Chételat, G. (2013). Hippocampal subfield volumetry in mild

cognitive impairment, Alzheimer's disease and semantic dementia. *NeuroImage: Clinical, 3*, 155-162. https://doi.org/10.1016/j.nicl.2013.08.007

Mawuenyega, K. G., Kasten, T., Sigurdson, W., & Bateman, R. J. (2013). Amyloid-beta isoform metabolism quantitation by stable isotope-labeled kinetics. *Analytical Biochemistry, 440*(1), 56-62. https://doi.org/10.1016/j.ab.2013.04.031

Moreta, M. P., Burgos-Alonso, N., Torrecilla, M., Marco-Contelles, J., & Bruzos-Cidón, C. (2021). Efficacy of acetylcholinesterase inhibitors on cognitive function in Alzheimer's disease: Review of reviews. *Biomedicines, 9*(11), Article 1689. https://doi.org/10.3390/biomedicines9111689

Oakley, H., Cole, S. L., Logan, S., Maus, E., Shao, P., Craft, J., Guillozet-Bongaarts, A., Ohno, M., Disterhoft, J., Van Eldik, L., Berry, R., & Vassar, R. (2006). Intraneuronal beta-amyloid aggregates, neurodegeneration, and neuron loss in transgenic mice with five familial Alzheimer's disease mutations: potential factors in amyloid plaque formation. *The Journal of neuroscience : the official journal of the Society for Neuroscience*, *26*(40), 10129–10140. https://doi.org/10.1523/JNEUROSCI.1202-06.2006

Qian, Z., Li, Y., & Ye, K. (2024). Advancements and challenges in mouse models of Alzheimer's disease. Trends in Molecular Medicine, 30(12), 1152-1164. https://doi.org/10.1016/j.molmed.2024.10.010

Rueden, C. T., Schindelin, J., Hiner, M. C., DeZonia, B. E., Walter, A. E., Arena, E. T., & Eliceiri, K. W. (2017). ImageJ2: ImageJ for the next generation of scientific image data. *BMC bioinformatics, 18*(1), 529. https://doi.org/10.1186/s12859-017-1934-z

Selkoe, D. J., & Hardy, J. (2016). The amyloid hypothesis of Alzheimer's disease at 25 years. *EMBO Molecular Medicine, 8*(6), 595–608. https://doi.org/10.15252/emmm.201606210

Stringer, C., Wang, T., Michaelos, M., & Pachitariu, M. (2021). Cellpose: a generalist algorithm for cellular segmentation. *Nature methods, 18*(1), 100–106. https://doi.org/10.1038/s41592-020-01018-x

Xu, D., Hopf, C., Reddy, R., Cho, R. W., Guo, L., Lanahan, A., Petralia, R. S., Wenthold, R. J., O'Brien, R. J., & Worley, P. (2003). Narp and NP1 form heterocomplexes that function in developmental and activity-dependent synaptic plasticity. *Neuron, 39*(3), 513–528. https://doi.org/10.1016/s0896-6273(03)00463-x

Yan, Y., Jiang, Y., Melcher, K., & Xu, H. E. (2017). Amyloid beta: Structure, biology and structure-based therapeutic development. *Acta Pharmacologica Sinica, 38*(9), 1205–1235. https://doi.org/10.1038/aps.2017.28

Ye, Q., Gast, G., Wilfley, E. G., Huynh, H., Hays, C., Holmes, T. C., & Xu, X. (2024). Monosynaptic rabies tracing reveals sex- and age-dependent dorsal subiculum connectivity alterations in an Alzheimer's disease mouse model. *The Journal of Neuroscience, 44*(16), e1796232024. https://doi.org/10.1523/JNEUROSCI.1796-23.2024

Zhao, W., Wang, X., Yin, C., He, M., Li, S., & Han, Y. (2019). Trajectories of the hippocampal subfields atrophy in Alzheimer's disease: A structural imaging study. *Frontiers in Neuroinformatics, 13*, Article 13. https://doi.org/10.3389/fninf.2019.00013